Validation of the plasma-wall self-organization model for density limit in ECRH-assisted start-up of Ohmic discharges on J-TEXT

Jiaxing Liu, Ping Zhu, Dominique Franck Escande, Junli Zhang, Donghui Xia, Yuhan Wang, Jiaming Wang, Qinghu Yang, Jiangang Fang, Xiaoqing Zhang, et al.

Validation of the plasma-wall self-organization model for density limit in ECRH-assisted start-up of Ohmic discharges on J-TEXT

Jiaxing Liu[1], Ping Zhu[1,2*], Dominique Franck Escande[3], Junli Zhang[1], Donghui Xia[1*], Yuhan Wang[1], Jiaming Wang[1], Qinghu Yang[1], Jiangang Fang[1], Xiaoqing Zhang[1], Li Gao[1], Zhifeng Cheng[1], Zhipeng Chen[1], Zhoujun Yang[1], Zhongyong Chen[1], Yonghua Ding[1], Yuan Pan[1] and the J-TEXT team‡

[1]International Joint Research Laboratory of Magnetic Confinement Fusion and Plasma Physics, State Key Laboratory of Advanced Electromagnetic Engineering and Technology, School of Electrical and Electronic Engineering, Huazhong University of Science and Technology, Wuhan, 430074, China.
[2]Department of Engineering Physics, University of Wisconsin-Madison, Madison, Wisconsin, 53706, United States of America.
[3]Aix-Marseille Université, CNRS, PIIM, UMR 7345, Marseille, France.
E-mails: zhup@hust.edu.cn, xiadh@hust.edu.cn

17 July 2023

Abstract. A recently developed plasma-wall self-organization (PWSO) model [D.F. Escande et al 2022 Nucl. Fusion 62 026001] predicts a significantly enhanced density limit, which may be attainable in tokamaks with ECRH-assisted Ohmic start-up and sufficiently high initial neutral density. Experiments have been conducted on J-TEXT to validate such a density limit scenario based on this model. Experimental results demonstrate that increasing the pre-filled gas pressure or ECRH power during the start-up phase can help effectively enhance plasma purity and raise the density limit at the flat-top phase. The experimental data shows that density limit increases by a ratio $0.76/0.6 \approx 1.27$ for a decrease by a factor $0.13/0.33 \approx 0.4$ in C_{III} radiation.

Keywords: Density limit, radiation, plasma wall interaction,ECRH, J-TEXT

1. Introduction

A high plasma density in a fusion device is crucial for fulfilling the Lawson criterion for ignition. However, there exists an upper limit to this density, above which a disruption may occur, leading to the termination of the discharge. Since this density limit sets a stringent

‡ See the author list of "N. Wang et al 2022 Advances in physics and applications of 3D magnetic perturbations on the J-TEXT tokamak, Nucl. Fusion 62 042016"

bound on the stable performance and ignition regimes of a tokamak, its scaling and the associated physics has been a subject of primary interests.

For decades, people used the empirical scaling law for the tokamak density limit $n_{\mathrm{G}}\left(\mathrm{m}^{-3}\right)=\dfrac{I_{\mathrm{p}}\left(\mathrm{MA}\right)}{\pi a\left(\mathrm{m}\right)^{2}}\times 10^{20}$, where I_{p} is the plasma current and a is the minor radius [1, 2]. Recently, a power balance model considering radiation introduced a modified scaling for the density limit, $(I_{\mathrm{p}}P/a^{4})^{(4/9)}$, where P is the heating power [3, 4, 5]. This radiative scaling is in better agreement with the tokamak and reversed field pinch (RFP) experimental databases as shown in Fig. 4 of [5] and [3], respectively. The same model yields a good scaling for the stellarator too [3, 5, 6]. The primary factors influencing these power balance limits stem from impurity radiation, which is largely controlled by plasma-wall interactions [3, 4, 5]. This radiation affects the amount of heat reaching the limiter/divertor targets, subsequently determining the temperature in the target region. Additionally, the target region temperature significantly impacts impurity production, which in turn influences impurity radiation. This feedback mechanism forms the foundation of the recently proposed plasma-wall self-organization theory [7]. This self-organization mechanism yields a steady level of impurity radiation only when the plasma density is below a certain radiative limit [7]. A higher density limit is reached in stellarator when the start-up is performed by using higher ECRH power [8, 9]. This higher density limit might be due to their mode of breakdown at start-up phase: the massive use of ECRH power with high neutral density producing less impurities [3, 7]. Furthermore, in W7-X the effective plasma charge Z_{eff} decreases with ECRH power [10]. This suggests that increasing progressively and simultaneously the ECRH power and the initial neutral density could also decrease the initial production of impurities in tokamaks [7]. And this may increase the above radiative density limit.

In order to investigate the impact of start-up conditions , including pre-filled gas pressure and ECRH power, on the flat-top density limit in ECRH assisted Ohmic discharges, a series of experiments are conducted on the J-TEXT tokamak. The experimental results indicate that increasing either the pre-filled gas pressure or the ECRH power in the start-up phase can help achieve leads to a reduction in impurity radiation, an increase in the boundary electron temperature during the flat-top phase, and an enhancement of the density limit in most of the shots. Meanwhile, the density limit is calculated using PWSO 0D and 1D model with parameters of J-TEXT. The results demonstrated a general agreement with the experimental data under certain parameter assumptions.

The remainder of this paper is organized as follows: Section 2 introduces the experimental set-up. Section 3 details the experimental methods and presents the measurement results. Section 4 offers a comparison and analysis of the experimental and calculated results. Lastly, Section 5 concludes with a summary and discussion.

2. Experimental set-up

The J-TEXT tokamak is a medium sized iron-core tokamak with a major radius $R_0 = 1.05\,\mathrm{m}$, minor radius $a = 25-29\,\mathrm{cm}$, and a silicon-carbide-coated graphite limiter [11, 12]. The

typical J-TEXT discharge in the limiter configuration is performed with a toroidal magnetic field B_t of $\sim 2.0\,\mathrm{T}$, a plasma current I_p of $\sim 200\,\mathrm{kA}$, plasma density n_e of $1-7\times10^{19}\mathrm{m}^{-3}$, and an electron temperature T_e of $\sim 1\,\mathrm{keV}$ [11, 12]. The Ohmic discharges begin with a reversed current closed at $t = 0.0\,\mathrm{ms}$ to increase the rate of magnetic flux change. Then the capacitors bank, including the ionization capacitors, discharges to the Ohmic coils to induce a toroidal electric field, ionizing the gas within the vacuum chamber. Following this, the capacitors for rapid build up of plasma current are turned on.

The material of limiter targets in J-TEXT is carbon whose chemical sputtering by hydrogen is not negligible in comparison to the physical sputtering [13]. The role of silicon carbide coating is to reduce the sputtering of carbon. In the following calculation concerning the sputtering function, its effects are neglected since the impurity radiation on J-TEXT primarily originates from carbon. The limiter target can absorb a large amount of gas in high electron density discharges, thus cleaning discharges have to be carried out during the experiments. Since non-standard start-up settings are used for this study, a noticeable amount of discharges fail or disrupt. Gas puffing can be applied to inject hydrogen with various pre-filled gas pressure and gas puffing rate. The ECRH system on J-TEXT was installed in 2019 [12, 14]. Generated by a gyrotron, the maximum output power is 500 kW and the frequency is 105 GHz. The toroidal magnetic field range of the ECRH system operation is $1.7\,\mathrm{T} \leq B_t \leq 2\,\mathrm{T}$. The ECRH auxiliary heating system operates at the second harmonic frequency with X mode [15, 16].

The primary diagnostics for this experiment include the photo-diode array (PDA), Langmuir probe, polarimeter-interferometer (Polaris) system, and vacuum gauge. The arrangement of these diagnostic systems, as viewed from the top, is depicted in Fig. 1. The PDA array, responsible for measuring C_{III} and hydrogen-alpha radiations on the high field side, comprises 18 channels installed at the top of port 10. A Langmuir probe array at port 13 measures the electron temperature around the top limiter. The Polaris system is capable of measuring 17-channel line-averaged plasma electron density at different major radii [17]. The vacuum gauge quantifies the pre-filled gas pressure within the vacuum vessel.

3. Experimental results

3.1. Baseline discharge

A pure Ohmic start-up baseline discharge is performed as a baseline discharge (#1082483) and its key parameters, including target region plasma temperature T_t, C_{III} and H_α radiation levels, plasma current I_p, ECRH power and normalized density n_e/n_G, are shown in Fig. 2. This discharge starts at 0.0 s, with a toroidal magnetic field of 1.875 T and a plasma current of 120 kA. Hydrogen gas is injected after an electric pulse is sent to the gas puffing system, resulting in a neutral gas pressure of approximately 3 mPa at $t = 0\,\mathrm{s}$. During the current plateau period, gas injection continues until the plasma density limit of $0.70n_G$ is reached. At this point, the plasma density starts to decrease and then rapidly drops to zero, without any prior manifestation of MHD activities. More experimental details can be found in recent

reports [15, 16].

3.2. Density limit parameter dependence

46 discharges were performed with varying pre-filled gas pressure and start-up ECRH power, 13 of which were on the first experimental day and 33 on the second. The key parameters and density limits of these discharges are shown in table B1 and B2 of Appendix B. Eight proper discharges are selected to obtain the dependence of density limit n_{limit} on key parameters including the target region plasma temperature T_{t} and the C_{III} radiation power. The selected discharges shown in Fig. 3 and Fig. 4 have identical plasma current, toroidal magnetic field but differ in start-up conditions, either in terms of pre-filled gas pressure or ECRH power. The plasma temperature T_{t} around the limiter target and impurity radiation power $R_{C_{III}}$ in Fig. 3 and Fig. 4 represent their average values over the time interval $[200\,\mathrm{ms}, 250\,\mathrm{ms}]$, during which they are relatively stable. The experimental data indicates that lower C_{III} radiation and higher target region temperature generally lead to a higher density limit. Experimentally, the C_{III} radiation and target region plasma temperature at the current plateau phase can be adjusted by changing the start-up conditions.

Experimentally, the density limit values achieved under identical or similar input conditions may differ due to the deterioration or evolving of device status, such as that of the wall. However, this does not affect the overall law of the experimental results and the comparison with the theory model, since the key of these experiments is changing the start-up conditions rather than the way in which they are changed. The change in start-up conditions consists of two aspects, on the one hand, the controllable input parameters, such as ECRH power and pre-filled gas pressure, and on the other hand the deterioration or evolution of difficult to control device conditions, such as wall conditions, which cannot be neglected especially in devices with carbon targets. From our existing experiments, it is clear that increasing the ECRH power or pre-filled gas pressure can help to increase the density limit, but this is not always effective, likely due to the evolving or deterioration of the wall conditions. Besides, all attempts with pre-filled gas pressure higher than 7.5 mPa did not start successfully, which may be attributed to the short mean free path of electrons in a too-high density neutral gas that is not able to achieve a sufficiently high ionization rate [18, 19]. In addition, too high a pre-filled pressure also requires more input energy to complete the burn-through process[20]. Increasing the ECRH power simultaneously at high pre-filled pressure might improve the probability of successful start-up. Subsequently, two typical examples of varying gas pressure and ECRH power will be discussed in detail.

3.3. Typical discharge for changing gas pressure

Discharge #1083014 is performed with a higher pre-filled gas pressure than the baseline discharge and key parameters is compared with baseline discharge in Fig. 2. First, the neutral gas pressure P_{neu} at $t = 0\,\mathrm{s}$ is approximately three times higher than that in baseline discharge and remains higher during the current ramping phase. Then, The C_{III} radiation power oscillates at the beginning of the current plateau phase and eventually approaches

a steady level over time in both discharges which suggest that there may be a time delay in the development of radiation as described in the PWSO model. And the target region plasma temperature is higher in the discharge with higher gas pressure after the radiation power stabilizes. This should be related to the lower radiation level which lead to more energy deposited on the limiter target in the higher pre-filled gas pressure discharge. During the current plateau phase, hydrogen gas is injected at the same rate until the density limit disruption is triggered. Finally, a higher density limit of $0.75n_{\mathrm{G}}$ is achieved in the discharge with higher pre-filled gas pressure.

3.4. Typical discharge for changing ECRH power

Another discharge, #1082481, is performed with the application of ECRH over the time interval $[-25\,\mathrm{ms}, 20\,\mathrm{ms}]$ and the key parameters is also plotted and compared in Fig. 2. The injected ECRH power is approximately 230 kW. Concurrently, the hydrogen gas is injected at the same rate with the baseline discharge until the density limit is reached. As seen in Fig. 2(d), the injected ECRH power before $t = 0\,\mathrm{s}$ ionizes the pre-filled gas and forms the so-called pre-plasma and leading to a higher target region plasma temperature subsequently. The $\mathrm{C_{III}}$ radiation power also oscillates initially and reaches a lower steady state than that of the baseline discharge. Then the steady target region plasma temperature remains higher which may result from higher radiation and then lower energy deposited on the limiter targets. During the current plateau phase, the plasma density in this discharge increases at nearly the same rate as that of the baseline discharge but for an extended duration, ultimately reaching a higher density limit of $0.76n_{\mathrm{G}}$.

4. Theory and experiment comparison

We further compare the predictions from the PWSO 0D and 1D models with the J-TEXT experimental results presented in the previous section.

4.1. PWSO 0D model and comparison

The basic idea of the PWSO theory (section 4.1 of [7]) is that the existence of a time delay in the feedback loop relating impurity radiation and impurity production on divertor/limiter plates yields a delay equation in the 0D model

$$R+ = \alpha(P-R) \tag{1}$$

where P is the total input power to plasma, R the total radiated power, and $R+$ the delayed radiation power during the next cycle of the feedback loop.

The coefficient α quantifies the radiation power $R+$ generated by the impurity produced from the plasma-wall interaction that is proportional to the deposition of the outflow power $(P-R)$ onto the wall targets, which is modeled as [7]

$$\alpha = \frac{f\lambda}{aD_{\perp}T_{\mathrm{t}}} I\left(T_{\mathrm{t}}\right) \int_0^a rn(r)\,\mathrm{Rad}[T(r)]\mathrm{d}r \tag{2}$$

where a is the plasma radius, n is the electron density, $D_\perp$ is the perpendicular diffusion coefficient, T_t is the plasma temperature at the target plate location, f is the fraction of the sputtered atoms that reach the main plasma and become ionized at a distance λ inwards from the plasma target location, $\mathrm{Rad}[T(r)] = \mathrm{Rad}[T]$ is the impurity radiation rate coefficient, $T = T(r)$ is the plasma temperature in the 0D model, and $I(T_\mathrm{t})$ is an average of the yield function of carbon $Y(E)$ over the energies of the impinging particles

$$I(T_\mathrm{t}) = \sqrt{\frac{m}{2\pi T_\mathrm{t}}} \int_0^\infty Y\left(\frac{mv^2}{2} + \gamma T_\mathrm{t}\right) \exp\frac{-mv^2}{2T_\mathrm{t}}\, \mathrm{d}v \tag{3}$$

where γ is the total energy transmission coefficient [13], γT_t is a measure of the Debye shield length, and m is the ion mass. The fixed point of Eq.(1) $R = R+$ corresponds to the plasma-wall self-organization equilibrium. The plasma-wall system is unstable for $\alpha > 1$ as predicted from Eq. (1). So the condition that the threshold $\alpha = 1$ establishes a radiation density limit

$$n_c = \frac{2D_\perp}{f\lambda\,\mathrm{Rad}[T]} \frac{T_\mathrm{t}}{I(T_\mathrm{t})\,a} \tag{4}$$

which can be reached for a ratio of total radiated power to total input power as low as 1/2 [7]. If there is a detachment, the plasma temperature at the plates decreases as shown in Fig. 5, which makes α to vanish, since sputtering does too. This pushes the radiative density limit to very high values, especially when physical sputtering dominates the contribution to radiation. There are two basins of PWSO at the flat top of plasma current. The usual one is the regime of density limit corresponding to the higher temperatures of targets, whereas the other is the regime of density freedom corresponding to the lower temperatures of targets, in particular in machines where the target plates are made of high-Z materials.

The projectile particles in our experiments are deuterons and the target material is carbon. The yield function consists of two parts for the physical and chemical sputtering contributions. The interpolating functions for $Y_\mathrm{phy}(E)$ at normal incidence are provided in the Eq. (15) of [21] for physical sputtering

$$Y_\mathrm{phy}(E) = 0.042 \frac{Q(Z_2)\,\alpha^*(M_2/M_1)}{U_\mathrm{s}} \frac{S_\mathrm{n}(E)}{1+\Gamma k_\mathrm{e}\varepsilon^{0.3}} \times \left[1 - \sqrt{\frac{E_\mathrm{th}}{E}}\right]^s \tag{5}$$

where the parameters on the right hand of Eq. (5) can also be found. Here the numerical coefficient 0.042 is in unit of $\mathrm{Å}^{-2}$, Z_1 and Z_2 are the atomic numbers, M_1 and M_2 are the masses of the projectile and the target atoms, respectively, S_n is the reduced nuclear stopping cross section, U_s is the surface binding energy of the target solid, k_e is the Lindhard electronic stopping coefficient, E is the projectile energy, E_th is the threshold energy for sputtering, ε is the reduced energy $E\frac{M_2}{M_1+M_2}\frac{a_L}{Z_1Z_2e^2}$, the Γ factor has the form $W(Z_2)/\left(1+(M_1/7)^3\right)$, and W and Q are dimensionless fitting coefficients. The yield function $Y_\mathrm{che}(E)$ for chemical sputtering is obtained from fitting the available experimental data in Fig. 3.8 of [13] and Fig. 6 of [22] using the least squares method

$$Y_\mathrm{l,che}(E) = \begin{cases} a_1E_\mathrm{l}^2 + b_1E_\mathrm{l} + c_1 & E_\mathrm{l} < E_\mathrm{l,inter} \\ a_2E_\mathrm{l} + b_2 & E_\mathrm{l} \geq E_\mathrm{l,inter} \end{cases} \tag{6}$$

where $E_{\mathrm{l}} = \log_{10}(E)$, $Y_{\mathrm{l,che}} = \log_{10} Y_{\mathrm{che}}$, Y_{che} represents the chemical sputtering yield function. a_1, b_1, c_1, a_2, b_2, and $E_{\mathrm{l,inter}}$ are the fitting coefficients. The values of these coefficients can be found in Appendix A, along with a plot illustrating the fitted chemical sputtering yield function and the original data points. For our experiments on J-TEXT, the minor radius $a = 0.265\,\mathrm{m}$, and the impurity radiation rate $\mathrm{Rad}[T]$ is assumed to be a constant value $10^{-32}\mathrm{Wm}^{-3}$ [4, 13]. We further assume that the perpendicular diffusion coefficient $D_\perp$ of target impurities is $0.01\mathrm{m}^2\mathrm{s}^{-1}$, and one percent of the sputtered atoms penetrate the main plasma, undergoing ionization at a distance $\lambda = 0.01\,\mathrm{m}$ away from the target. The maximum energy carried by the projectile particle is assumed to be $5000\,\mathrm{eV}$, which is needed in the integral operation of Eq. (3). The relation between the density limit and the temperature of target for our experiments as predicted by the PWSO 0D model is thus calculated and shown in Fig. 6.

The PWSO 0D model predicts a density-free regime ($T_{\mathrm{t}} \lesssim 2\,\mathrm{eV}$) and a density-limit regime ($T_{\mathrm{t}} \gtrsim 2\,\mathrm{eV}$). In the density-free (density-limit) regime, the density limit increases with the decrease (increase) of the target region plasma temperature. J-TEXT experimental results are located in the density-limit regime, which qualitatively agree with the PWSO 0D model predictions.

4.2. PWSO 1D model and comparison

A more detailed evolution of the radiation power and the temperature towards the PWSO equilibrium profiles can be obtained from the PWSO 1D model (see appendix C of [7]).

The impurity density and the plasma temperature evolution can be determined from the following 1D transport equations

$$\partial_t n_i - D\partial_x^2 n_i = C_i \left[\partial_x T\left(r_{\mathrm{LCFS}}, t - \tau_{\mathrm{delay}}\right) + T'_{\mathrm{loss}}\right] \delta(x - a + \lambda)\,, \tag{7}$$

$$n\partial_t T - K\partial_x^2 T = C_T T^{3/2} + P_{\mathrm{add}} - n n_i \mathrm{Rad}(T)\,, \tag{8}$$

where $C_i = -\frac{faKI(T_{\mathrm{t}})}{(a-\lambda)T_{\mathrm{t}}}$ represents the plasma-wall interaction, K is a uniform diffusion coefficient, $C_T = \frac{E_0^2}{\eta(T)T^{3/2}} \simeq 6.510^2 \frac{E_0^2}{Z}$, with E_0 the electric field corresponding to the loop voltage, $\eta(T)$ is the transverse Spitzer resistivity, and P_{add} is the additional power density. The above parameters of J-TEXT are used to obtain the following results and the resistivity η is considered to be a constant. Applying the following initial and boundary conditions

$$\begin{aligned} &n_i(x=a) = 0; \quad \left.\frac{\partial n_i}{\partial x}\right|_{x=0} = 0 \\ &T(x=a) = T_0; \quad \left.\frac{\partial T}{\partial x}\right|_{x=0} = 0 \\ &n_i(t=0) = 0; \quad T(t=0) = T_0 \end{aligned} \tag{9}$$

a relation between the density limit and the target region temperature has been obtained and compared with the experimental data as shown in Fig. 6.

The PWSO 1D model also predicts the existence of a density-limit basin and a density-free basin. The J-TEXT experimental data are located in the density limit basin, as in the

case of the 0D model. Within the density-limit basin, altering the start-up condition, such as increasing the pre-filled gas pressure and ECRH power at the start-up phase, should result in lower C_{III} radiation power, indicating a cleaner plasma, which leads to a higher density limit. The higher target region plasma temperature is likely a consequence of the higher power flux in the SOL, due to lower radiation inside the plasma. Additionally, The 0D and 1D models have opposite trade offs. The former is very simplistic and the latter is more elaborated, but with more parameters, whose experimental value is not precisely known. Experimental values between the corresponding two curves is an encouraging fact.

The lower C_{III} radiation power when using ECRH at sart-up confirms the improvement of purity expected in [7] due to a central breakdown of the discharge.

5. Summary

In this work, the density limits predicted from the 0D and 1D PWSO models are compared and validated with the J-TEXT experimental data, which are located in the density-limit basin and demonstrate quantitative agreement with the PWSO model predictions under some parameter assumptions. Both theory and experiment suggest that a higher density limit corresponds to a lower impurity radiation state, which could be reached through increasing either the ECRH power or the pre-filled gas pressure at the start-up phase. In fact, due to the easy absorption of gases by carbon targets and other experimental conditions, it is difficult to start a discharge out of J-TEXT's usual start-up conditions. So, experimentally, increasing either the ECRH power or the pre-filled gas pressure at the start-up phase may not be always efficient in changing the start-up conditions. In contrast, experiments in a tokamak with tungsten targets might enter deeply the density-free regime. Furthermore, metallic walls should enable scans of initial neutral gas density and of ECRH power with less failures and disruptions at start-up than with carbon ones.

In future, we plan to carry out more experiments to explore whether or how the J-TEXT tokamak can operate in the density-free basin predicted by the PWSO model. In the meantime, this model is being implemented in a more complete transport simulation code to predict and interpret the experimental process in a more realistic way.

6. Acknowledgment

This work is supported by the National MCF Energy R&D Program of China under Grant Nos. 2019YFE03050004 and 2018YFE0310300, the National Natural Science Foundation of China Grant No. 51821005, and the U.S. Department of Energy Grant Nos. DE-FG02-86ER53218 and DE-SC0018001. The computing work in this paper is supported by the Public Service Platform of High Performance Computing by Network and Computing Center of HUST.

Appendix A. The fitted chemical sputtering yield function

The data used to fit Eq. 6 are from Fig. 3.8a of [13] and Fig. 6 of [22]. The values of fitting coefficients are as follows: $a_1 = -0.21716823, b_1 = 1.49621640, c_1 = -3.10869745, a_2 = -0.55766667, b_2 = -0.88506667$, and $E_{\mathrm{l,inter}} = 1.24709069$. And Fig. 7 shows the plot of original data used and the fitting function.

Appendix B. Key parameters of the experiments

The key discharge parameters of the different shots on experimental day 1 and 2 are listed in table B1 and table .B2.

References

[1] M. Greenwald, J.L. Terry, S.M. Wolfe, S. Ejima, M.G. Bell, S.M. Kaye, and G.H. Neilson. A new look at density limits in tokamaks. Nuclear Fusion, 28(12):2199–2207, 1988.

[2] M. Greenwald. Density limits in toroidal plasmas. Plasma Physics and Controlled Fusion, 44(8):R27–R53, 2002.

[3] P. Zanca, F. Sattin, D.F. Escande, G. Pucella, and O. Tudisco. A unified model of density limit in fusion plasmas. Nuclear Fusion, 57(5):056010, 2017.

[4] P. Zanca, F. Sattin, D.F. Escande, and JET Contributors. A power-balance model of the density limit in fusion plasmas: application to the L-mode tokamak. Nuclear Fusion, 59(12):126011, 2019.

[5] P. Zanca, F. Sattin, D.F. Escande, F. Auriemma, and JET Contributors. A power-balance model for the L-mode radiative density limit in fusion plasmas. Plasma Physics and Controlled Fusion, 64(5):054006, 2022.

[6] G. Fuchert, S.A. Bozhenkov, N. Pablant, K. Rahbarnia, Y. Turkin, A. Alonso, T. Andreeva, C.D. Beidler, M. Beurskens, A. Dinklage, J. Geiger, M. Hirsch, U. Höfel, J. Knauer, A. Langenberg, H.P. Laqua, H. Niemann, E. Pasch, T. Sunn Pedersen, T. Stange, J. Svensson, H. Trimino Mora, G.A. Wurden, D. Zhang, R.C. Wolf, and W7-X Team. Global energy confinement in the initial limiter configuration of Wendelstein 7-X. Nuclear Fusion, 58(10):106029, 2018.

[7] D.F. Escande, F. Sattin, and P. Zanca. Plasma-wall self-organization in magnetic fusion. Nuclear Fusion, 62(2):026001, 2022.

[8] T. Klinger, T. Andreeva, S. Bozhenkov, C. Brandt, R. Burhenn, and B. Buttenschon et al. Overview of first Wendelstein 7-X high-performance operation. Nuclear Fusion, 59(11):112004, 2019.

[9] R.C. Wolf, A. Alonso, S. Akaslompolo, J. Baldzuhn, M. Beurskens, C.D. Beidler, and C. Biedermann et al. Performance of Wendelstein 7-X stellarator plasmas during the first divertor operation phase. Physics of Plasmas, 26(8):082504, 2019.

[10] A. Pavone, U. Hergenhahn, M. Krychowiak, U. Hoefel, S. Kwak, J. Svensson, P. Kornejew, V. Winters, R. Koenig, M. Hirsch, K.-J. Brunner, E. Pasch, J. Knauer, G. Fuchert, E.R. Scott, M. Beurskens, F. Effenberg, D. Zhang, O. Ford, L. Vanó, and R.C. Wolf. Measurements of visible bremsstrahlung and automatic Bayesian inference of the effective plasma charge Zeff at W7-X. Journal of Instrumentation, 14(10):C10003, 2019.

[11] Y. Liang, N. Wang, Y. Ding, Z. Chen, Z. Chen, Z. Yang, Q. Hu, Z. Cheng, L. Wang, Z. Jiang, B. Rao, Z. Huang, Y. Li, W. Yan, D. Li, H. Liu, L. Zeng, Y. Huang, D. Huang, Z. Lin, W. Zheng, F. Hu, K. Zhao, M. Jiang, Y. Shi, H. Zhou, S. Peng, W. Guo, L. Gao, Z. Wang, M. Zhang, K. Yu, X. Hu, Q. Yu, G. Zhuang, K. Gentle, Y. Pan, and the J-TEXT Team. Overview of the recent experimental research on the J-TEXT tokamak. Nuclear Fusion, 59(11):112016, 2019.

[12] N. Wang, Y. Liang, Y. Ding, Z. Chen, Z. Chen, Z. Yang, D. Xia, W. Zheng, W. Yan, D. Li, Z. Jiang, L. Wang, B. Rao, Q. Hu, X. Zhang, J. Zhang, X. Chen, X. Xu, T. Xu, X. Xie, Z. Huang, F. Mao, D. Han,

J. Li, T. Wang, L. Liu, R. Tong, Z. Lin, Y. Wei, N. Cai, Y. Shi, Y. Zhang, W. Guo, X. Zhang, P. Shi, Z. Cheng, P. Zhu, M. Liu, S. Ma, Y. Yang, C. Li, L. Gao, Z. Wang, M. Zhang, K. Yu, X. Hu, Q. Yu, K.W. Gentle, Y. Pan, and the J-TEXT Team. Advances in physics and applications of 3D magnetic perturbations on the J-TEXT tokamak. Nuclear Fusion, 62(4):042016, 2022.

[13] P. C. Stangeby. The Plasma Boundary of Magnetic Fusion Devices. CRC Press, 2000.

[14] D. Xia, F. Cui, C. Liu, Z. Wang Z. Yu, Y. Jin, and the J-TEXT team. The anode power supply for the ECRH system on the J-TEXT tokamak. Plasma Science and Technology, 20(1):014018, 2018.

[15] J. Zhang, P.D. Vries, K. Nagasaki, D. Xia, W. Jiang, and Z. Wang. Electron cyclotron heating assisted start-up experiments in J-TEXT. IEEE Transactions on Plasma Science, 48(12):4397–4501, 2020.

[16] J. Zhang, P. D. Vries, K. Nagasaki, D. Xia, W. Jiang, Z. Yang, Z. Cheng, L. Gao, X. Xu, Z. Wang, N. Wang, Y. Ding, Z. Chen, Z. Chen, P. Yuan, and J-TEXT Team. Experimental study of the electron cyclotron heating assisted start-up on J-TEXT. Nuclear Fusion, 63(7):076028, 2023.

[17] Y. Wang, L. Gao, P. Shi, X. Xu, Y. Zhou, Q. Yang, C. Yang, Q. Tao, C. Shen, Y. Wang, L. Wang, Z. Chen, D. Xia, Z. Chen, N. Wang, Z. Yang, Y. Ding, Y. Pan, and J-TEXT Team. Recent progress on the J-TEXT three-wave polarimeter-interferometer. Plasma Science and Technology, 24(6):064001, 2022.

[18] B. Lloyd, G.L. Jackson, T.S. Taylor, E.A. Lazarus, T.C. Luce, and R. Prater. Low voltage Ohmic and electron cyclotron heating assisted startup in DIII-D. Nuclear Fusion, 31(11):2031, 1991.

[19] D. Mueller. The physics of tokamak start-up. Physics of Plasmas, 20(5):058101, 2013.

[20] P.D. Vries and Y. Gribov. ITER breakdown and plasma initiation revisited. Nuclear Fusion, 59(9):096043, 2019.

[21] Y. Yamamura and H. Tawara. Energy dependence of ion-induced sputtering yields from monatomic solids at normal incidence. Atomic Data and Nuclear Data Tables, 62(2):149–253, 1996.

[22] J. Roth, E. Tsitrone, and A. Loarte. Plasma–wall interaction: Important ion induced surface processes and strategy of the EU Task Force. Nuclear Instruments and Methods in Physics Research Section B: Beam Interactions with Materials and Atoms, 258(1):253–263, 2007.

Table B1. The key discharge parameters of the different shots on experimental day 1 listed in chronological order. The first column indicates the experimental day on which the discharge was performed. The second column is the experimental discharge number. The third, fourth, and fifth columns are the ECRH power, the pre-filled gas pressure at $t = 0\,\mathrm{s}$, and the density limit, respectively. The last column is a short description of the corresponding discharge.

Exp day	shot number (108xxxx)	P_{EC} (kW)	P_{neu} (mPa)	density limit (n_{G})	notes
day 1	2478-2480	200	2.5	/	To find a proper gas puffing at plateau phase.
	2481	200	2.5	0.76	/
	2482	200	2.5	0.72	/
	2483	0	2.5	0.70	/
	2484	0	2.5	0.70	Repeat 1082483; radiation data is not available.
	2485	0	24	/	Increase P_{neu}; disruption at start-up phase.
	2486,2487,2489	/	/	/	Cleaning shots.
	2488, 2490	0	24	/	Repeat 1082485; disruption at start-up phase.

Table B2. The key discharge parameters of the different shots on experimental day 2 listed in chronological order. The first column indicates the experimental day on which the discharge was performed. The second column is the experimental discharge number. The third, fourth, and fifth columns are the ECRH power, the pre-filled gas pressure at $t = 0\,\mathrm{s}$, and the density limit, respectively. The last column is a short description of the corresponding discharge.

Exp day	shot number (108xxxx)	P_{EC} (kW)	P_{neu} (mPa)	density limit (n_{G})	notes
day 2	2984-2989	$200 \sim 300$	2.5, 5.5	/	Recover discharge and test ECRH system.
	2990-2992	/	/	/	Cleaning shots
	2993	200	5.5	0.59	/
	2994	0	5.5	0.61	No ECRH compared with 1082993
	2995	300	5.5	0.57	Different ECRH power.
	2996	100	5.5	0.60	Different ECRH power.
	2997	200	12.0	/	Increase P_{neu}; disruption at start-up phase.
	2998-3000	/	/	/	Cleaning shots.
	3001	200	12.0	/	Repeat 1082997; disruption at start-up phase.
	3002-3004	200	4.0, 5.5, 7.5	/	Decrease P_{neu}; no disruptions.
	3005	200	7.5	/	Repeat 1083004; disruption at start-up phase.
	3006, 3007	/	/	/	Cleaning shots.
	3008	200	7.5	/	Repeat 1083004; no disruption.
	3009	200	7.5	/	Repeat 1083004; disruption at start-up phase.
	3010,3011,3013	/	/	/	Cleaning shots.
	3012	200	7.5	0.75	Increase P_{neu} at plateau phase based on shot 1083009; radiation data is unavailable.
	3014	0	7.5	0.74	No ECRH compared with shot 1083012.
	3016	200	11.0	/	Increase P_{neu}; disruption at start-up phase.
	3018	300	11.0	/	Increase P_{EC}; disruption at start-up phase.
	3015,3017	/	/	/	Cleaning shots.

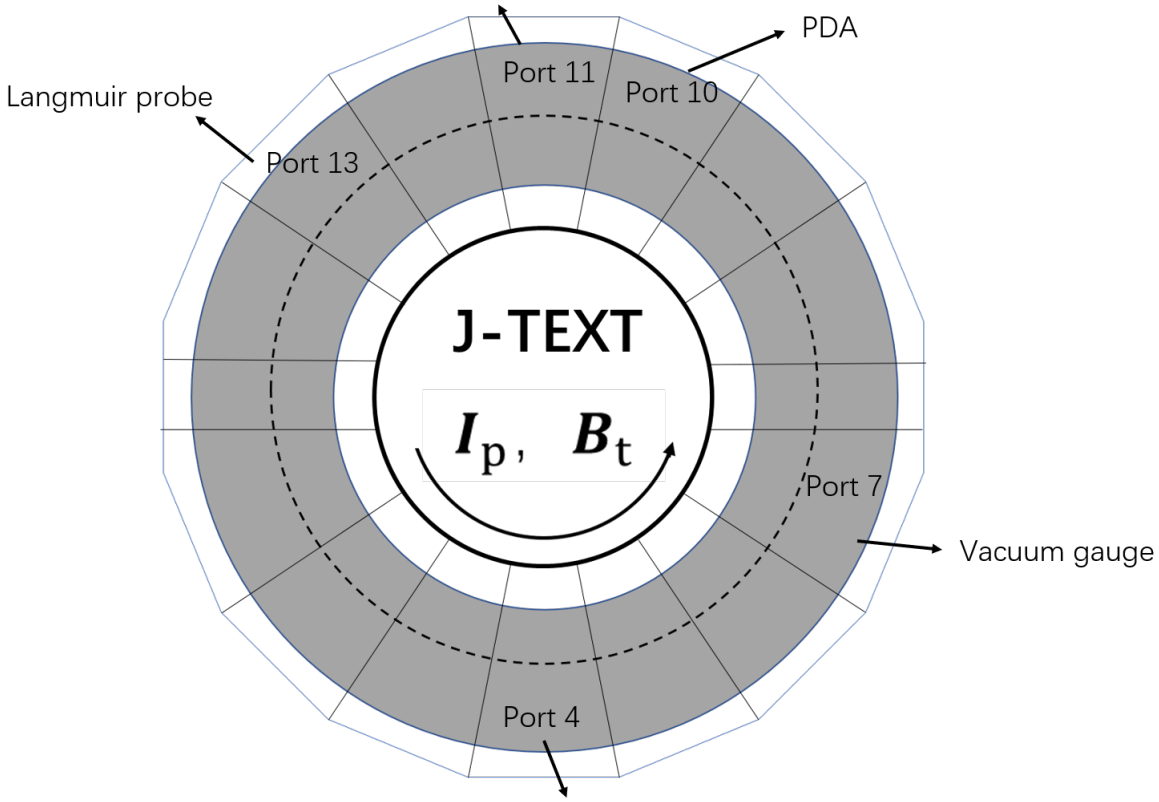

Figure 1. Top view of the relevant diagnostics on J-TEXT utilized in this study.

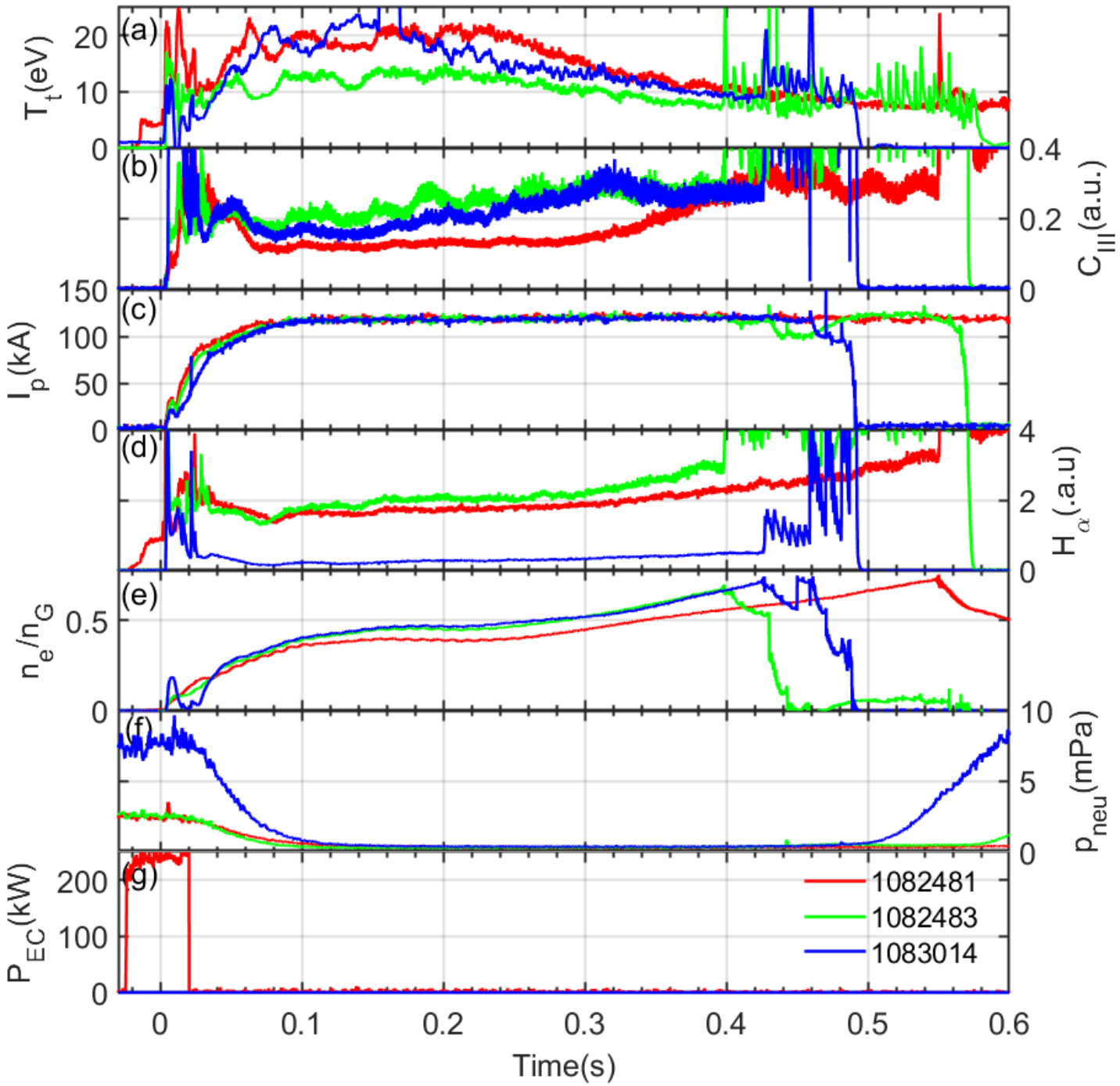

Figure 2. Time histories of key parameters in density limit experiments with different ECRH power and pre-filled gas pressure in the start-up phase. Blue: a pure Ohmic start-up baseline discharge, green: a discharge with higher pre-filled gas pressure, red: a discharge with ECRH $P_{EC} \approx 230$ kW at start-up phase. (a): the target region plasma temperature measured by a Langmuir probe installed on the limiter target. (b): the relative intensity of C_{III} radiation measured by PDA at 144mm from the centre of the circle to the centre of the chord. (c): Plasma current. (d): the relative intensity of hydrogen-alpha radiation measured by PDA which reflects the ionization condition of working gas, namely hydrogen gas. (e): the plasma electron density normalized by the Greenwald density limit. (f): The neutral gas pressure in the vessel measured by vacuum gauge. (g): The injected ECRH power.

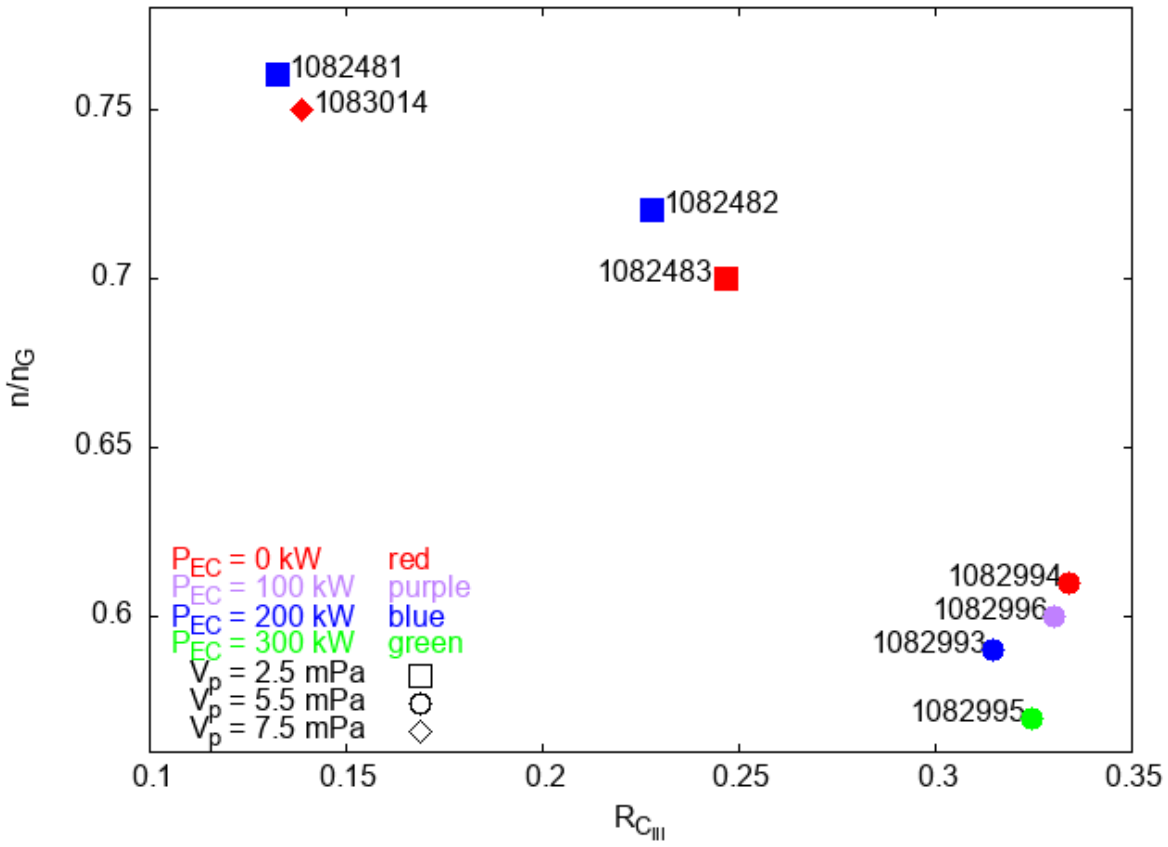

Figure 3. The density limit and the corresponding radiation power $R_{C_{III}}$ measured from experiments for varying ECRH power and pre-filled gas pressure in the start-up phase.

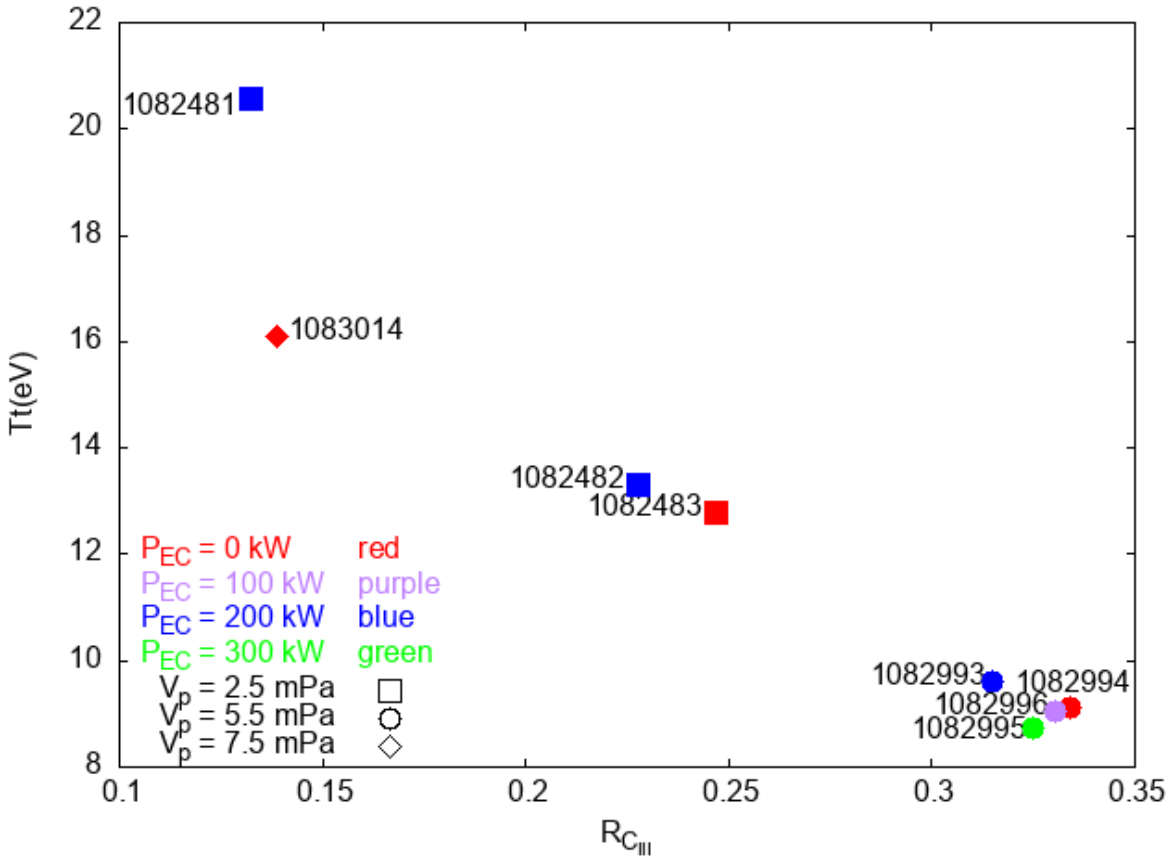

Figure 4. The plasma target region temperature T_t and the corresponding impurity radiation power $R_{C_{III}}$ measured from experiments for varying ECRH power and pre-filled gas pressure in the start-up phase.

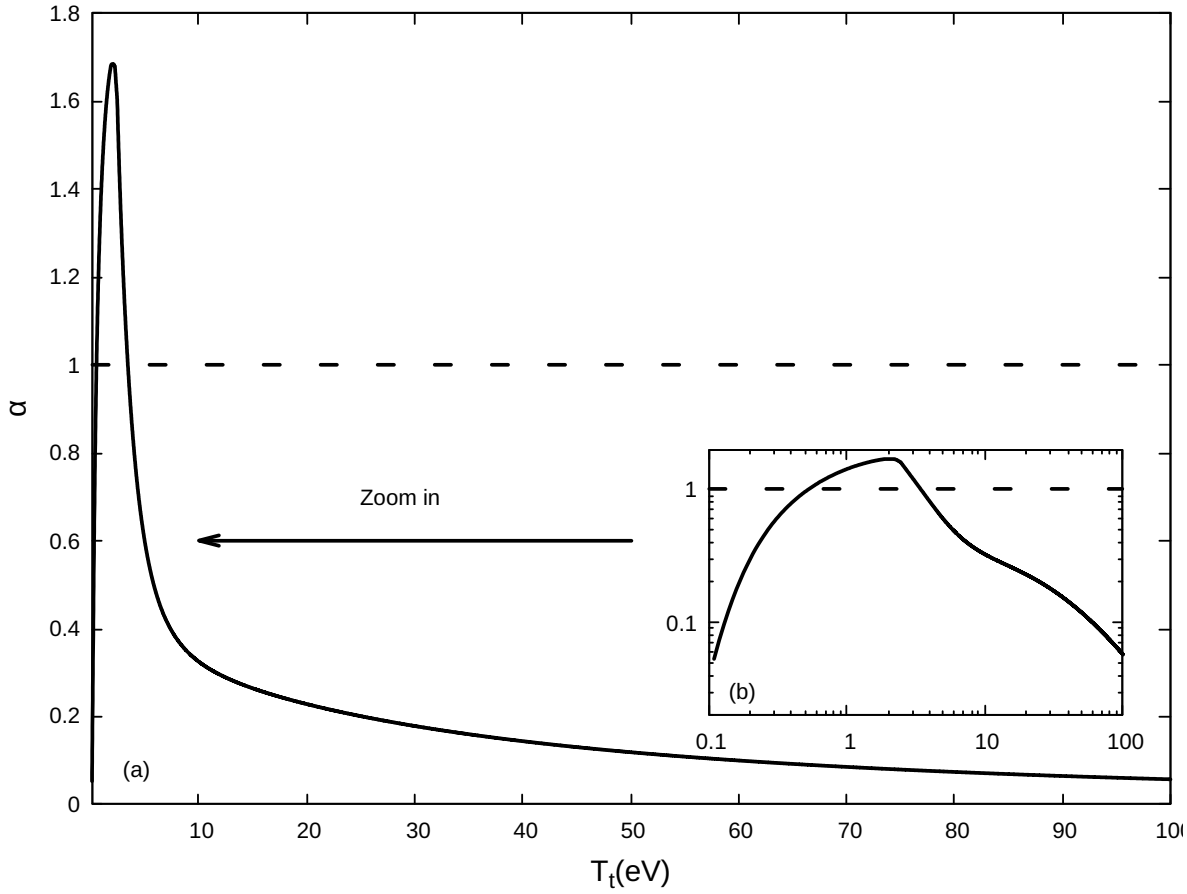

Figure 5. The coefficient α in Eq. (2) of the PWSO 0D model as a function of the target region plasma temperature using (a): linear and (b): logarithmic coordinates for a fixed plasma density.

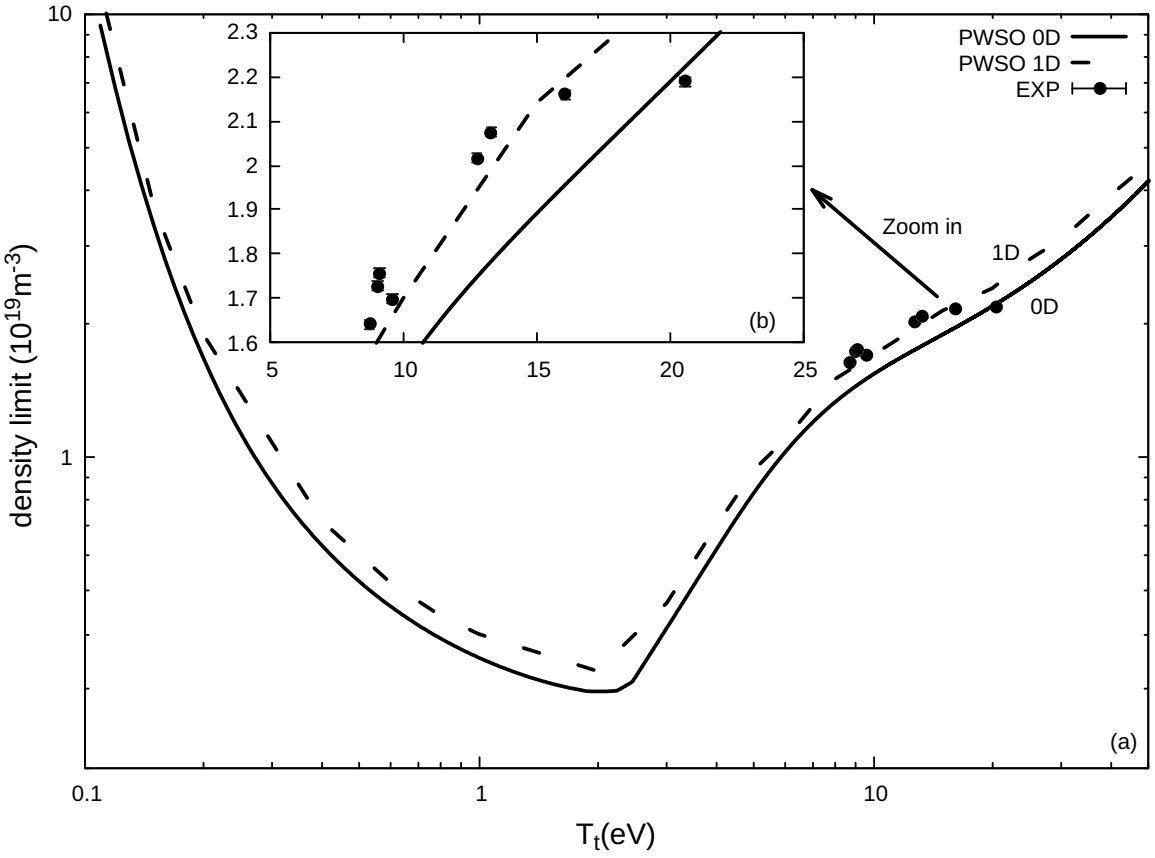

Figure 6. The density limits as functions of the target region plasma temperature T_t using (a): logarithmic and (b): linear coordinates as predicted from the PWSO 0D (solid line) and 1D (dashed line) models in comparison with the experimental data (circular symbol) where the error bars represent the electron density measurement error.

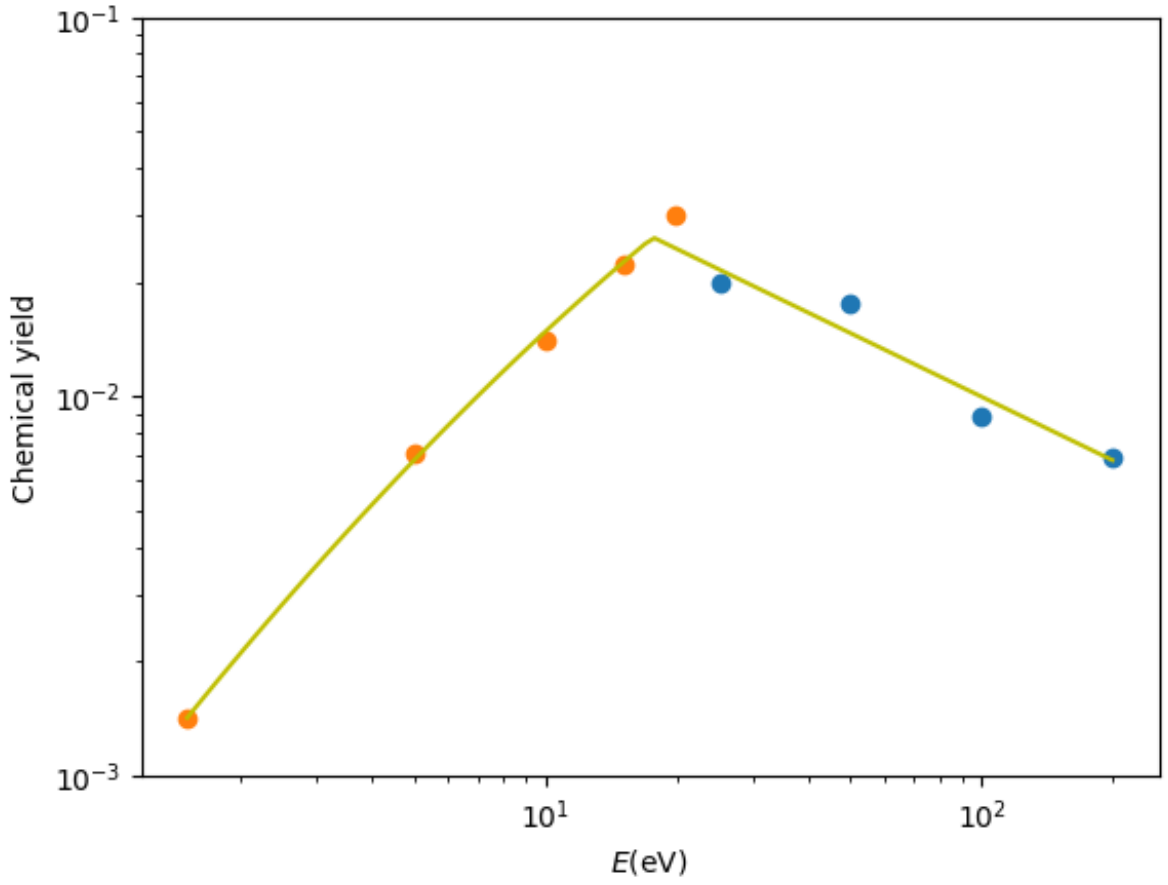

Figure 7. The fitted chemical sputtering yield function (solid line) and the original data from [13] (blue points) and [22] (orange points).